POLITECNICO DI TORINO
Repository ISTITUZIONALE

Impact of WIVERN Wind Observations on ARPEGE Numerical Weather Prediction Model Forecasts Using an Ensemble of Data Assimilation Method

Original
Impact of WIVERN Wind Observations on ARPEGE Numerical Weather Prediction Model Forecasts Using an Ensemble of Data Assimilation Method / Sasso, N., Borderies, M., Chambon, P., Berre, L., Girardot, N., Moll, P., Payan, C., Pourret, V., Battaglia, A., Illingworth, A., Rennie, M., Pourshamsi, M.. - In: QUARTERLY JOURNAL OF THE ROYAL METEOROLOGICAL SOCIETY. - ISSN 0035-9009. - 151:770(2025). [10.1002/qj.4991]

Availability:
This version is available at: 11583/3002183 since: 2025-07-28T15:59:01Z

Publisher:
John Wiley and Sons Ltd

Published
DOI:10.1002/qj.4991

Terms of use:

This article is made available under terms and conditions as specified in the corresponding bibliographic description in the repository

Publisher copyright
Wiley postprint/Author's Accepted Manuscript

This is the peer reviewed version of the above quoted article, which has been published in final form at http://dx.doi.org/10.1002/qj.4991.This article may be used for non-commercial purposes in accordance with Wiley Terms and Conditions for Use of Self-Archived Versions.

(Article begins on next page)

26 November 2026

ORIGINAL ARTICLE

Journal Section

Impact of WIVERN wind observations on Arpege NWP model forecasts using an Ensemble of Data Assimilation method

Nicolas Sasso[1] | Mary Borderies[1] | Philippe Chambon[1] | Loïk Berre[1] | Nicole Girardot[1] | Patrick Moll[1] | Christophe Payan[1] | Vivien Pourret[1] | Alessandro Battaglia[2] | Anthony Illingworth[3] | Michael Rennie[4] | Maryam Pourshamsi[5]

[1]CNRM UMR 3589, Météo-France/CNRS, Toulouse, France

[2]Dipartimento di Ingegneria dell'Ambiente, del Territorio, Politecnico di Torino, Turin, Italy

[3]Department of Meteorology, University of Reading, Reading, UK

[4]ECMWF, Reading, UK

[5]ESA-ESTEC, Noordwijk, Netherlands

Correspondence
Mary Borderies, CNRM, Météo-France, CNRS, Toulouse, France
Email: mary.borderies@meteo.fr

Funding information

To fill the gap of in-cloud wind observations in the global observing system, ESA has selected the WIVERN mission as one of the Earth Explorer 11 candidate missions to enter Phase A in 2023. WIVERN, with its dual-polarisation Doppler conically scanning W-band radar, will be the first space-based mission to provide in-cloud Horizontal Line-of-Sight (HLOS) winds at a fine vertical resolution of 650 m sampling and a broad swath of width 800 km. This article reports on the impact of WIVERN simulated HLOS winds to improve global Numerical Weather Prediction (NWP) model forecasts, using an Ensemble of Data Assimilation (EDA) approach. In this methodology, the benefits of adding WIVERN simulated HLOS wind observations to the current observing system are measured by their ability to reduce the EDA spread at a given forecast lead time. The operational EDA system of the global NWP model ARPEGE (Action de Recherche Petite Echelle Grande Echelle) is used for a one-month period in 2021. Results indicate that WIVERN HLOS will not only significantly improve the uncertainty of the wind forecasts throughout the entire troposphere, but also of the temperature and humidity fields. This positive impact is particularly seen in the mid-latitudes. Results of this study also highlight the strong vertical complementarity between WIVERN, Aeolus (Doppler wind lidar) and Atmospheric Motion Vectors observations. Finally, the impact of WIVERN is also studied in synergy with the EUMETSAT follow-on EPS-Aeolus mission, and results demonstrate that the two active wind satellite missions would vertically complement each-other as they provide wind observations at different altitude, and in different meteorological areas.

Keywords: WIVERN, Earth-Explorer 11, data assimilation, EDA, cloud radar, wind

1 | INTRODUCTION

Numerical Weather Prediction (NWP) models are operationally used on a daily basis to provide accurate predictions of weather forecasts at global and at regional scales. The quality of these forecasts strongly depends on the initial atmospheric state. Among the various observations very useful to NWP, several studies have shown that the assimilation of wind observations was beneficial for analyses and forecasts (Baker et al., 2014; Horányi et al., 2015). In addition, Li et al. (2023) reassessed the importance of wind observations rather than mass observations in reducing forecast errors in the tropics. Nevertheless, the percentage of wind observations in the Global Observing System (GOS) is less than 10% of the total number of assimilated observations in global NWP centres (Horányi et al., 2015).

Atmospheric Motion Vector (AMV) winds are derived operationally from the motion of cloud and water vapour tracers in successive satellite images acquired from the geostationary orbits or low Earth orbit. They provide wind data measurements on a global scale with a very high temporal resolution. As shown by a recent Observing System Experiments (OSEs) experiments, AMV observations are particularly useful in the lower and high troposphere (Chambon et al., 2023), and especially at short-range forecasts (Bormann et al., 2019; Chambon et al., 2023). However, unlike most active sensors, AMV measurements do not provide vertical wind profiles but only cloud top information with an uncertainty in the knowledge of the observed cloud-top altitude (Salonen et al., 2015). Scatterometer observations are also operationally assimilated in most NWP centres, and their impact is kept at long forecast ranges (Chambon et al., 2023). However, they provide only surface wind observations, and their influence is limited to the lower levels. Airborne have the advantage of collecting a large data set of wind observations over land and sea on very fine scales. However, except in the vicinity of airports where they provide profiles of wind observations during take-off and landing, they are only available at the flight altitude. Profiles of wind observations are also provided by profilers and radiosonding, but they are limited in space and time. Therefore, there is a lack of wind observations in the global observing system.

To provide global observations of vertical wind profiles, in 2018 the European Space Agency (ESA) launched the Aeolus satellite (Aeolus) mission (Reitebuch, 2012). Aeolus carries the first space-borne Doppler Wind lidar, providing Horizontal-Line-of-Sight (HLOS) wind observations throughout an atmospheric column in clear and cloudy conditions (top of optically thick clouds and within optically thin clouds) in the troposphere and in the lower stratosphere. Most meteorological centres have demonstrated the benefits of assimilating Aeolus HLOS observations in their global NWP models to reduce forecast errors (see for instance: Rennie et al., 2021; Pourret et al., 2022; Garrett et al., 2022; Martin et al., 2023) and several NWP centres operationally assimilated the data, which is unusual for a short demonstration mission. Despite its limited horizontal coverage (it only observes a two-dimensional curtain along the satellite track), Aeolus is one of the instruments with the largest positive impact per observation on global NWP forecasts (Rennie et al., 2021; Pourret et al., 2022). Although to a lesser extent, a slight positive impact of the assimilation of Aeolus wind profiles in the kilometre-scale NWP model Harmonie-Arome was also found by Hagelin et al. (2021). Recent studies have also shown the potential of Aeolus to improve tropical cyclone intensity forecasts (Marinescu et al., 2022; Garrett et al., 2022). In the light of these positive results, EUMETSAT is proposing an operational follow-on mission EPS-Aeolus (or Aeolus-2), which would also carry in 2034 a new European Doppler Wind Lidar (Marseille et al., 2023; Lean et al., 2023). The plan is for two satellites, one after the other covering roughly a decade. Several studies demonstrated the benefits brought by the assimilation of EPS-Aeolus in global NWP model using an Observing System Simulated Experiment (OSSE, Marseille et al., 2023) and an Ensemble of Data Assimilation (EDA, Lean et al., 2023; Healy et al., 2023) methods. As with Aeolus, these data will be limited to clear sky areas, as well as in the cloud top

of optically thick clouds and within thin clouds. Therefore, EPS-Aeolus is mainly designed to fill the gap in the global wind observing system in clear sky areas in the troposphere and the lower stratosphere.

Within clouds and precipitation, ground-based Doppler precipitation radar data provide positive impacts on kilometre-scale NWP models on rainy days (Montmerle and Faccani, 2009; Simonin et al., 2014; Ridal et al., 2023). However, these wind observations are limited to land and coastal areas, and to countries which are equipped with a radar network. Over the ocean, data assimilation experiments performed using research aircraft have demonstrated the benefits of assimilating Doppler radar data within clouds and precipitation (Sippel et al., 2014; Borderies et al., 2019a). However, these in-cloud wind observations cannot be used on a day-to-day basis to improve global NWP models. Consequently, there is a major gap of tropospheric wind data measurements on a global scale within clouds and precipitation.

To help fill this gap, WIVERN (WInd VElocity Radar Nephoscope Illingworth et al., 2018; Battaglia et al., 2022; Tridon et al., 2023) has been selected by ESA to enter in phase A in November 2023 as one of the two Earth-Explorer 11 candidates. Carrying a dual-polarisation, conically scanning, 94 GHz Doppler radar with a 800 km swath, WIVERN would provide the first profiles of winds within clouds and precipitation on a global scale with a quasi-daily revisit time on average. Observed with an off-zenith viewing angle of 42°and at a horizontal resolution of 20 km, the slanted HLOS wind profiles would complement the profiles measured by EPS-Aeolus in areas that are inaccessible to a Doppler wind lidar which is strongly attenuated by the upper layers of most clouds. A major advantage of WIVERN is also its sampling characteristics. Its wide cycloidal swath of 800 km would allow for quick collection of a large number of global wind and microphysical profiles. As an example, Tridon et al. (2023) demonstrated the ability of WIVERN to detect 50 times more cloudy observations than the nadir-looking cloud radar CloudSat in Tropical Cyclones with the baseline specified in phase 0.

The primary objective of this article is to evaluate, for the first time, the impact of the assimilation of WIVERN HLOS wind profiles in a global NWP model. The article also investigates the impact of the synergy of WIVERN with other real wind observations (AMV, Aeolus) and then with respect to the upcoming EPS-Aeolus follow-on mission. To assess the impact of WIVERN and EPS-Aeolus, an Ensemble of Data Assimilation (EDA) method is used. This method has been used at ECMWF since 2007 for research purposes to assess the impact of future types of observations in a NWP model (Tan et al., 2007; Harnisch et al., 2013; Lean et al., 2022; Healy et al., 2023). This approach was indeed initially proposed by Tan et al. (2007) for the preparation of the Aeolus mission, and then followed by Harnisch et al. (2013) to assess the impact of the expected increasing number of GNSS radio occultation measurements over the decade 2010-2020. The results obtained by Harnisch et al. (2013) were verified 10 years later by Lonitz et al. (2021) using real GNSS-RO observations. Following the successes obtained using the EDA method, it has recently been used by Lean et al. (2022) to assess the future EPS-STERNA constellation of small satellites carrying microwave sounders, and then by Healy et al. (2023) to assess the impact of EPS-Aeolus. The current impact study is carried out using the global operational EDA system of Météo-France, called Assimilation d'Ensemble ARPEGE "AEARP" (Desroziers et al., 1999), in which simulated WIVERN observations are assimilated jointly with real observations from the 2021 global observing system.

This article is organised as follows. section 2 describes the EDA framework used to assess the impact of WIVERN HLOS wind simulated observations. The EDA framework is then validated in section 3 by comparing the impact of real versus simulated Aeolus observations. The impact of WIVERN is evaluated and compared with respect to real

Aeolus and AMV wind observations in section 4. Finally, the zonal and vertical complementarity between EPS-Aeolus and WIVERN is demonstrated in section 5. Conclusions and perspectives are then given in section 6.

2 | IMPACT ASSESSMENT FRAMEWORK

2.1 | General description of the EDA method

To assess the impact of WIVERN on Numerical Weather Prediction (NWP) models, an Ensemble of Data Assimilation (EDA) method (Tan et al., 2007; Harnisch et al., 2013; Lean et al., 2022; Healy et al., 2023) is used. Unlike Observing System Simulation Experiments (OSSEs), which can also assess the impact of observations in a future NWP context (Duruisseau et al., 2017; Coopmann et al., 2023; Rivoire et al., 2024) but require all observing systems to be simulated from a so-called "nature run" (outputs of a model simulation representing the "truth"), the EDA approach only needs new observations to be simulated. These simulated observations are then assimilated along with all the available real observations from the global observing system. The EDA method is very close to information content studies based on Degree of Freedom for Signal (DFS), which measure the capacity of an observing system to reduce an a priori error, used for example for channel selection of satellite radiances (Birman et al., 2017). In the EDA approach, the positive impact of the simulated observations is measured by their ability to reduce the EDA spread at analysis time and also at other forecast lead times. In other words, in this approach, the impact is not studied in terms of forecast error reduction, such as for OSSEs, but in terms of estimated uncertainty (e.g. EDA spread) reduction. Recent studies performed at ECMWF (Duncan et al., 2021; Lean et al., 2022; Lonitz et al., 2021) conducted Observing System Experiments (OSEs) on real observations to provide evidence of the links between the EDA spread reductions and forecast error reductions. Results indicate that the EDA spread reduction is in good agreement with the forecast error reduction, suggesting that the EDA approach is a suitable method for assessing the impact of a new type of observation, as long as the random error characteristics are well known, although with a tendency to underestimate it due to the known underdispersive nature of the EDA.

A general description of the EDA method used for the WIVERN impact study is given in Figure 1. It requires several ingredients:

- The nature run represents the true state of the atmosphere and is used to simulate the future set of observations (e.g. WIVERN and/or Aeolus). It consists of analyses of the global operational 6h cycling 4D-Var assimilation system of Météo-France, called ARPEGE (Bouyssel et al., 2022). It is described in subsection 2.2.
- A forward operator to simulate WIVERN observations (described in subsection 2.3) from the nature run, to which appropriate observation errors and perturbations are then applied (see subsection 2.4).
- A global EDA system (described in subsection 2.5) in which these simulated observations are assimilated together with real observations. The positive impact of these simulated observations will then be assessed by their ability to reduce the EDA spread, compared to the EDA experiment in which WIVERN is not assimilated.

Each of these different ingredients of the EDA method is described in more detail in the following sections.

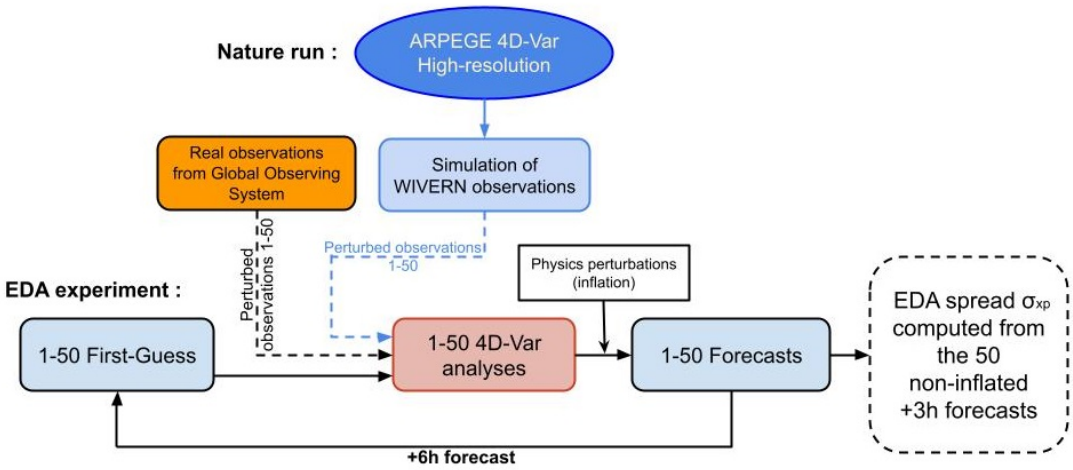

FIGURE 1 Description of the framework of the EDA method used to assess the impact of WIVERN.

2.2 | Nature Run

To simulate the WIVERN HLOS wind observations, analyses of the Météo-France operational global NWP model ARPEGE (Bouyssel et al., 2022) at high resolution (5 km over Western Europe to 25 km at the antipodes over New Zealand) are considered to represent the true state of the atmosphere. ARPEGE has 105 vertical levels, ranging from ~10 m above the ground to the model top at 0.1 hPa (~70 km). Initial conditions are provided four times a day by an incremental 4D-Var system (Courtier et al., 1994), which is cycled every six hours. The Ensemble Data Assimilation of ARPEGE (Desroziers et al., 1999, AEARP), described in subsection 2.5, is used to compute the background error covariance matrix. In ARPEGE, six types of hydrometeors are used to represent clouds and precipitation. Four of them are prognostic variables (stratiform snow, stratiform rain, cloud liquid water and cloud ice) and their evolution is governed by the microphysical scheme of Lopez (2002) and two of them (convective snow and convective rain) are diagnosed variables and governed by the deep convective scheme of Tiedtke (1989).

2.3 | WIVERN observation simulations

ARPEGE analyses are interpolated at WIVERN time and location to simulate WIVERN observations.

The first step in simulating WIVERN HLOS wind observations, is to identify the scenes where WIVERN will observe clouds or precipitation (i.e., where the radar reflectivity is greater than the WIVERN single-pulse radar sensitivity of -15 dBZ). The space-borne radar simulator which was recently included in version 13 of RTTOV-SCATT (Geer et al., 2021; Mangla et al., 2024) is used to simulate WIVERN W-band reflectivities. The inputs of the forward operator are ARPEGE profiles of temperature, pressure, specific humidity, hydrometeor contents, hydrometeor fractions and sensor parameters (e.g. radar frequency and viewing angle). Attenuation by moist air and hydrometeors is accounted for to compute the attenuated reflectivity. An in-depth description of the spaceborne radar simulator of RTTOV-SCATT is provided in Mangla et al. (2024). To save computation time, bulk scattering properties are stored in look-up tables, which were generated using the ARTS database (Eriksson et al., 2018) for frozen hydrometeors and Mie for drops. First, these simulated reflectivity values are used to keep only the cloudy scenes as observed by WIVERN,

with a reflectivity threshold of -15 dBZ. Then, they are used to prescribe realistic HLOS wind observation errors (see subsection 2.4).

Finally, a simple "point" HLOS wind observation operator, derived from the one already developed for the assimilation of Aeolus HLOS winds (Rennie et al., 2021; Pourret et al., 2022) is used to simulate HLOS wind profiles. Given the ARPEGE horizontal velocities (zonal wind u and meridional wind v, in m.s^{-1}) and the azimuth angle α, the HLOS wind is derived at an observation height z following Equation 1:

$$HLOS(z) = -u(z)\sin(\alpha) - v(z)\cos(\alpha) \tag{1}$$

Figure 2 shows the spatial locations of WIVERN simulated observations over the globe at three different altitude (from top to bottom panels), during a 6 hour assimilation window, between September 15, 2021,1500 UTC and September 12, 2021, 2100 UTC. The swath width of the satellite is represented by the lines surrounding the observations. WIVERN simulated reflectivities Z,in dBZ, are shown in Figure 2 (left column) at three different altitudes z, in km. The reflectivity values are only shown above the minimum detectable reflectivity of WIVERN (e.g. -15 dBZ). At $z \approx 8$ km (bottom panels), observations mainly come from the higher layers of the clouds where reflectivity values are smaller in the mid-latitudes than that at an altitude of $z \approx 4$ km (middle panels). At an altitude of $z \approx 4$ km, observations come from layers of the clouds with larger hydrometeor contents, compared to $z \approx 8$ km, which explains the increase in terms of reflectivity values. At lower altitude at $z \approx 3$ km, and in areas where reflectivity is large at $z \approx 4$ km (see for instance over Europe), reflectivity values are smaller, due to the strong attenuation of the signal by drops at W-band. Figure 2 (right column) shows the HLOS wind values of the simulated WIVERN observations over the globe, for the same three different altitudes.

2.4 | WIVERN data assimilation setup

2.4.1 | Resolution and thinning

The horizontal and vertical resolutions of simulated WIVERN observations are the same as the nature run. The high density of WIVERN observations, which will be available at approximately every 20 km with the settings specified for the Phase 0 baseline, is reduced in order to satisfy assumptions about observation error covariances on the horizontal. Indeed, they are assumed to be 0 $m\ s^{-1}$. This assumption holds for observations from different instruments with independent observation errors, but it may no longer be valid if the observations are collected very close to each other by the same instrument. It is therefore necessary to perform a thinning by decreasing the density of observations in order to have satisfactory assumptions about the covariances of the observation errors (Liu and Rabier, 2002). It has been decided to select one column out of four along and across tracks, which is equivalent to a distance of approximately 65 km.

2.4.2 | Quality control

Because WIVERN data will probably be affected by ground clutters, data below an altitude of 1.5 km is not assimilated in this study. However, it should be noted that this threshold is probably too pessimistic as, because of its slanted viewing angle, over ocean WIVERN would be less affected by ground clutters than any other current or future spaceborne radar which typically observe profiles of reflectivities at nadir or close to the nadir. Therefore, in this study, the impact of WIVERN is probably underestimated in the lower levels of the troposphere.

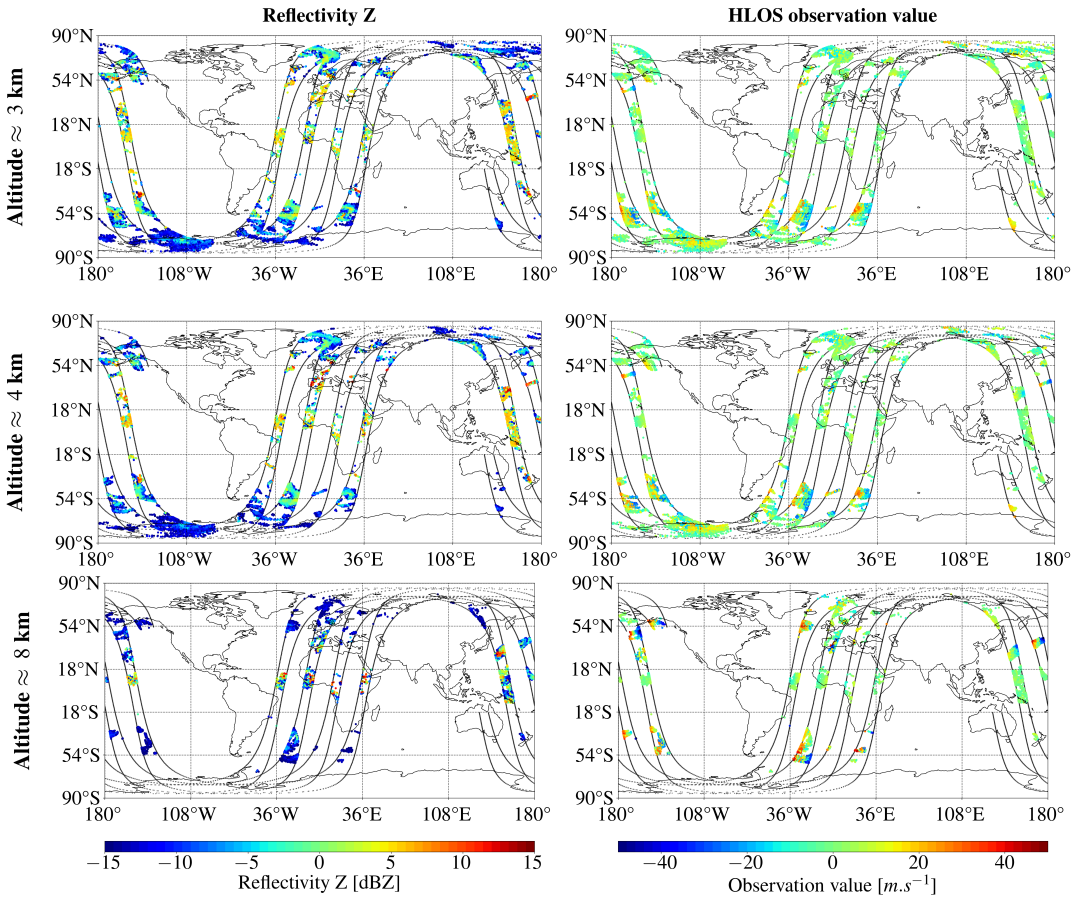

FIGURE 2 Reflectivity values (left column) and HLOS wind values (right column) of simulated WIVERN observations over the globe, between September 15, 2021,1500 UTC and September 15, 2021, 2100 UTC.

HLOS wind observations for which the reflectivities are less than the radar sensitivity of -15 dBZ are not assimilated.

2.4.3 | Observation error standard deviation

An in-depth description of the different sources of error in WIVERN Wind measurements can be found in Tridon et al. (2023). In this study, a simplified version of the standard deviation error is employed. For instance, errors associated to cross-talk echos between the H and the V pulses (Rizik et al., 2023) are not accounted for in this study. Indeed, the version 13.2 of the forward operator RTTOV-SCATT does not include the ability to simulate ghost echos yet. Besides, these echos will only slightly increase the noise of the Doppler velocities, and will be easily identified and filtered out in the measurements (Rizik et al., 2023).

Here, the variance of Line-Of-Sight (LOS) radar Doppler velocity decreases with the Signal to Noise Ratio (SNR) and is defined as (Pazmany et al., 1999; Battaglia et al., 2022):

$$\sigma_{LOS}^2 = \frac{1}{N}\frac{v_{Nyq}^2}{2(\pi\beta)^2}\left(\left(1+\frac{1}{SNR}\right)^2 - \beta^2\right) \tag{2}$$

with

$$SNR = 10^{(Z-Z_{min})/10} \tag{3}$$

$$\beta = e^{-\frac{1}{2}\frac{\pi^2\sigma_v{}^2}{v_{Nyq}{}^2}} \tag{4}$$

$$v_{Nyq} = \frac{\lambda}{4\,T_{HV}} \tag{5}$$

where $\lambda = 3$ mm is the radar wavelength, $T_{HV} = 20$ µs is the delay between two polarized pulses H and V, $N = 80$ is the number of pulse pairs (related to the integration length), $\sigma_v = 4$ m.s^{-1} is the Doppler spectral width, and v_{Nyq} is the Nyquist interval. Based on the phase 0 WIVERN specifications, WIVERN sensitivity Z_{min} has been set to -15 dBZ.

To account for Non-Uniform Beam Filling (NUBF), Wind-Shear (WS) and mispointing errors, the variance of LOS radar velocity observation error is increased by a correction factor c_1^2. These errors are expected to contribute to less than 1 m.s^{-1} in total (Battaglia et al., 2022; Tridon et al., 2023). The resulting corrected LOS standard deviation error $\sigma_{LOS,c}$ is defined as :

$$\sigma_{LOS,c}^2 = \sigma_{LOS}^2 + c_1^2 \tag{6}$$

with $c_1 = 1$ m.s^{-1} a correction factor considered as a maximal threshold (Battaglia et al., 2022; Tridon et al., 2023).

HLOS wind observation error is then derived following Equation 7:

$$\sigma_o = \sqrt{(\sigma_{LOS,c}/\sin(\theta))^2 + c_2^2} \tag{7}$$

where $\theta = 41.6$ ° is the incidence angle, and $c_2 = 1$ m.s^{-1} is introduced to take into account the uncertainty on vertical motion of the flow during the conversion of the LOS to the HLOS wind. Figure 3 shows the evolution of WIVERN HLOS observation error standard deviation as a function of the reflectivity.

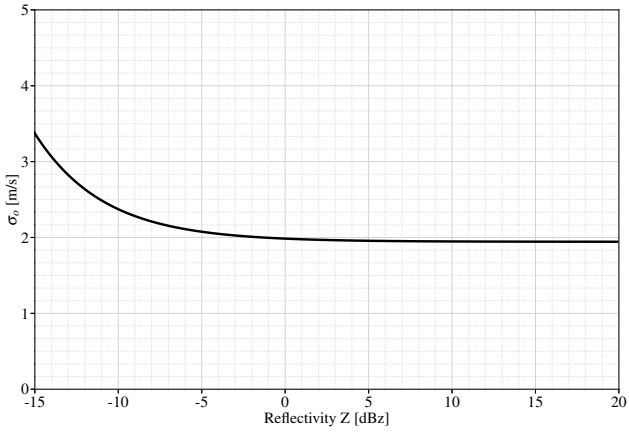

FIGURE 3 WIVERN HLOS observation error standard deviation σ_o(in $m\ s^{-1}$) as a function of the reflectivity simulated using RTTOV-SCATT.

2.5 | EDA details: The EDA system of Météo-France

The EDA system of Météo-France (Desroziers et al., 1999), called Assimilation d'Ensemble ARPEGE "AEARP", is run operationally since 2008 to estimate flow-dependent background error covariances for the deterministic 4D-Var assimilation system of the ARPEGE deterministic global model (Bouyssel et al., 2022) as well as to initialize the ARPEGE Ensemble Prediction System. The current system consists of 50 members each one running a simplified four-dimensional variational (4D-Var) data assimilation system every six hours at low resolution, as compared to its deterministic configuration. For each member of the ensemble, the minimization is performed at 100 km with only one inner-loop. Unlike for the deterministic ARPEGE model (see subsection 2.2), the forecasts are predicted at a fixed horizontal resolution of 40 km.

The 50 members of the ensemble are generated by only perturbing the observations (**?**) and by applying a multiplicative inflation factor to each forecasts of the ensemble to account for model errors (Raynaud et al., 2012). This inflation factor depends on the variable, and is a function of the ratio between a climatological spread for each variable, and the ensemble spread calculated at a given assimilation time. As this inflation procedure could influence the observation impact, the EDA spread values are calculated on the non-inflated forecasts.

Here, the EDA experiments are fully cycled. The background error covariance matrix B of each EDA experiment is a flow-dependent matrix calculated using the fifty members of each EDA experiment. Therefore, it is not fixed and varies with the meterological situation and with the observing system. This allows to account for a reduction in B, linked with an improved observing system.

2.6 | Period of study

Due to the stable characteristics of the EDA (Tan et al., 2007; Harnisch et al., 2013), the EDA experiments are only performed for a period of one month. September 2021 is chosen as the period of study. As in the studies of Lean et al. (2022) and Healy et al. (2023), the first week of the simulated period of study is removed to calculate the EDA

spread ratio, in order to allow each EDA experiment to spin up. Thus, the period of study extends from 15/09/2021 to 08/10/2021 (21 days).

It should be noted that Aeolus had a relatively low Signal to Noise Ratio (SNR) during this period (transmission loss with FM-B laser), meaning that the Rayleigh-clear winds were very noisy and the Mie-cloudy winds had less spatial coverage, but it remains in the top 3 of the observing systems with the greatest impact per observation in terms of the Forecast Sentivity to Observations index (FSOi).

2.7 | Used metric: the EDA spread ratio

To compare the impact of the new observations on the EDA spread σ_x of a model variable x at an altitude z, the normalized difference of spread ratio I_x is introduced in Equation 8:

$$I_x(z) = \frac{\sigma_{x,XP}(z) - \sigma_{x,REF}(z)}{\sigma_{x,REF}(z)} * 100 \tag{8}$$

where $\sigma_{x,REF}$ denotes the ensemble spread of a reference experiment REF, and $\sigma_{x,XP}$ the averaged ensemble spread of an other experiment XP, which typically includes new observations. The subscript x stands for the model variables on which the EDA spread is calculated (e.g. zonal wind u, meridional wind v, temperature T, and specific humidity q).

Here, only short range forecasts (e.g. below 12h) are used to compare the different experiments. Indeed, the EDA method is not well suited to study the impact at longer range forecasts because, as the forecast range increases, the impact of the observations becomes less significant than forecast model uncertainties (Harnisch et al., 2013). To ease the comparisons with other studies (Lean et al., 2022; Healy et al., 2023), the spread ratios are only shown for a forecast range of +12 hours.

3 | VALIDATION OF THE EDA FRAMEWORK USING AEOLUS-1 OBSERVATIONS

The same validation method as in Healy et al. (2023) is employed using real HLOS wind observations from the 2021 global observing system. In particular, as Aeolus-1 and WIVERN observe the same wind product (e.g. HLOS winds), the validation of the methodology is conducted by comparing the impact of real versus simulated Aeolus-1 observations.

3.1 | Simulation of Aeolus-1 observations

The identical spatial geolocation (altitude, longitude, latitude) and temporal information as for the real Aeolus-1 observations are used to simulate Aeolus-1 observations. They are interpolated at the time and location of the same ARPEGE analyses used to simulate WIVERN HLOS observations (see subsection 2.2 for further details). The same forward operator as the one used for WIVERN HLOS wind observations is employed (see Equation 1). Given the azimuth angle (provided by the real Aeolus-1 dataset), ARPEGE zonal u and meridional v wind components are projected onto the HLOS view of Aeolus-1 to simulate Aeolus-1 HLOS wind.

3.2 | Data assimilation set-up for the simulated Aeolus-1 observations

In order to mimic as closely as possible the impact of real Aeolus-1 observations, the same data assimilation setup as for Aeolus-1 is followed. This setup is further described in Pourret et al. (2022). The along-track sampling is ≈ 80 km for Rayleigh clear winds, and of ≈ 12 km for Mie-Cloudy winds.

A simulated Aeolus-1 observation is classified as Mie-Cloudy (resp. Rayleigh-clear) if it is the case in the real observations. This assumption allows to maintain consistency with the full observing system and the weather systems (clear versus cloudy meteorological scenes). Therefore, if Aeolus-1 identified the scene as Mie-Cloudy (resp. Rayleigh-Clear) in the observations, a Mie-Cloudy (resp. Rayleigh-Clear) observation error is assigned to that simulated pixel. An in-depth description of the observation error standard deviation for Aeolus-1 is provided in Pourret et al. (2022). The average vertical profiles of observation errors are also depicted in red in Figure 8 for this specific period of study.

3.3 | Comparison of the impact of real versus simulated Aeolus-1 observations

To validate the methodology, three EDA experiments are performed.

- The REF experiment includes the full 2021 operational observing system (eg. AMVs, passive observations, scatterometers, conventional observations etc..), but by discarding Aeolus-1 observations;
- A second experiment includes, on top of the same observations used in the REF experiment, the real Aeolus-1 observations;
- The last experiment includes, on top of the same observations used in the REF experiment, the simulated Aeolus-1 observations.

The REF experiment is used as a reference to calculate the EDA spread ratio for the real and the simulated Aeolus-1 experiments. The vertical profiles of zonal wind spread ratio I_u (resp. meridional wind spread ratio I_v) for the two Aeolus experiments are shown in the top panels (resp. bottom panels) of Figure 4 in the Northern Hemisphere (left), Tropics (middle) and Southern Hemisphere (right). Negative values of spread ratios indicate a reduction of the ensemble spread in the new EDA experiment, which means that the new observation (e.g. simulated or real Aeolus-1 observations) has been able to reduce the uncertainty of the 12 hour forecasts. Therefore, negative values indicate a positive impact of the assimilation of the corresponding new observations.

The two curves are in very good agreement with each other, meaning that the impact of simulated Aeolus-1 observations on the spread ratio is of the same order of magnitude as the impact of real Aeolus-1 observations. Consistently with the results found by Healy et al. (2023), this gives us confidence in the employed methodology (combination of the nature run and error characteristics for the simulated observations), and in the impact obtained for WIVERN and further described below in section 4.

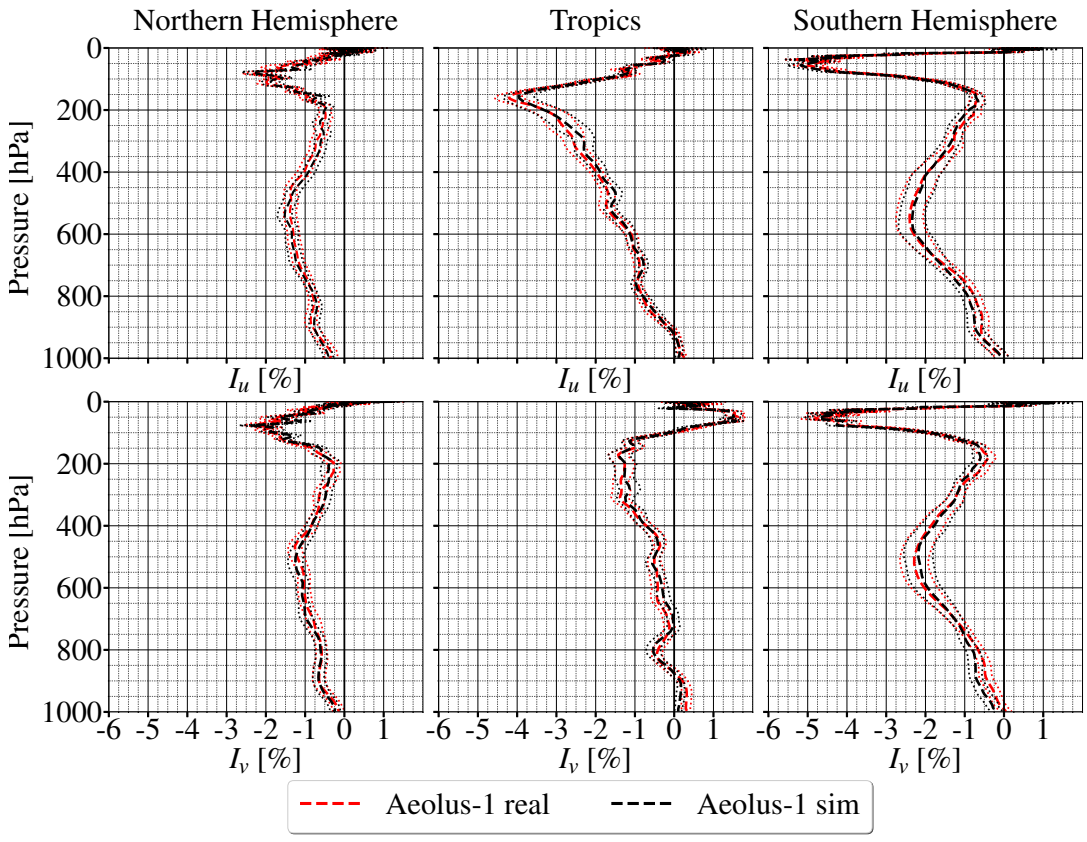

FIGURE 4 Vertical profiles of EDA spread ratio for zonal wind I_u (top) and meridional wind I_v (bottom), for the real Aeolus-1 observations (red dotted line), and the simulated Aeolus-1 observations (black dotted line). These profiles are shown for the Northern Hemisphere (left), Tropics (middle) and Southern Hemisphere (right). Spread ratio profiles are computed with 12 hour forecasts and averaged over the 21 days period of study. Dotted lines surrounding the main colored lines represent the interval of confidence of 99%.

4 | COMPARISONS OF THE IMPACT OF WIVERN VERSUS REAL OBSERVATIONS (AMVS AND AEOLUS)

In this section, the impact of WIVERN is evaluated and compared with respect to other real spaceborne wind observations which are typically assimilated in the mid and upper troposphere (e.g. Aeolus-1 and AMVs).

4.1 | EDA experiments

To assess the impact of AMV, Aeolus-1 and WIVERN wind observations, a total of seven EDA experiments are run for the period of study. The reference EDA experiment (*REF*) includes the assimilation of the 2021 operational observing system (e.g. scatterometers, radiosondes, aircraft data, passive microwave and IR observations, etc...), but by discarding Aeolus-1 and AMV observations. In addition to this baseline, three more experiments are carried out to assess separately the impact of AMVs, Aeolus-1 and WIVERN onto the EDA spread. Next, to assess the complementarity of WIVERN with Aeolus-1 and AMV observations, two more experiments are performed in which WIVERN is assimilated jointly with either Aeolus-1 or AMV observations. Finally, the three instruments are assimilated together (on top of the baseline of the *REF* experiment) in the last EDA experiment. The seven experiments are summarized in Table 1.

Experiment \ Observations	WIVERN	AMVs	Aeolus-1	Other
REF				x
AMVs		x		x
Aeolus-1			x	x
WIVERN	x			x
WIVERN + AMVs	x	x		x
WIVERN + Aeolus-1	x		x	x
WIVERN + AMVs + Aeolus-1	x	x	x	x

TABLE 1 Description of the observations used in the different EDA experiments of the study. AMV wind observations are derived from geostationnary (METEOSAT 9/11, HIMAWARI-8, GOES-16(E), GOES-17(W)) and polar (NOAA 15/18/19, Terra/Aqua) satellites. "Other" stands for all the other observations used operationally in the Météo-France ARPEGE model: conventional observations (e.g. radiosondes, drifting buoys, pilot land report, synop stations, Land stations and ships, european wind profiler, etc...), aircraft report, passive microwave (e.g. AMSU-A, MHS, AMSR-2, GMI, ATMS, SSMIS, SAPHIR, MWHS-2) and infrared (IASI, SEVIRI, AHI, CRIS) observations in clear sky areas, scatterometer observations (ASCAT), GNSSRO observations.

4.2 | Comparison of the number of observations

The AMVs, Aeolus-1 and WIVERN EDA experiments are first compared in terms of number of assimilated observations at each assimilation time.

The average numbers of daily assimilated observations during the period of study are shown in Table 2. For ease

of comparisons, the numbers are also given as percentages (bottom row in Table 2), using the total number of the observations made by the three instruments as the reference. Aeolus-1 observations are shown for Mie-Cloudy and Rayleigh-Clear scenes. First, Table 2 shows that the number of Aeolus-1 observations is much higher in clear-sky (e.g. Rayleigh Clear) areas than in cloudy (e.g. Mie-Cloudy) areas (1.5% versus 5.8%). Next, the large number of AMVs observations (27.5%) is explained by the large number of geostationary (up to 5) and polar-orbiting (up to 5) satellites from which these observations are available. Finally, Table 2 shows that, although WIVERN is only assimilated in cloudy and precipitating areas, the largest proportion of observations comes from WIVERN (65%). This large number of observations comes from its large 800 km wide conical sampling, but also from its ability to provide in-cloud wind observations at a high vertical resolution.

Instrument	Aeolus-1 Mie	Aeolus-1 Rayleigh	AMVs	WIVERN
Number of observations	31960	118623	562390	1334928
Percentage of observations	1.5%	5.8%	27.5%	65%

TABLE 2 Average number of daily assimilated observations for Aeolus-1, AMVs and simulated WIVERN observations in ARPEGE model for a 1-month period.

The zonal average daily number of observations is depicted as a function of the pressure level in Figure 5 for Aeolus-1 in Mie-Cloudy (upper left) and Rayleigh-Clear (upper right) conditions, AMV (bottom left) and simulated WIVERN (bottom right) observations. As expected, the number of Aeolus-1 observations predominates in clear-sky areas at all latitudes, compared to the cloudy areas. Next, Aeolus-1 Mie-cloudy observations are mainly located in the troposphere, where there are clouds. As shown in Figure 5 (top right panel), the majority of Aeolus-1 observations in Rayleigh-Clear conditions are in the upper atmosphere, where the pressure level is below 500 hPa, and in the stratosphere. In the lower layers of the atmosphere, above a pressure level of approximately 800 hPa, all of the assimilated Aeolus observations are in Mie-Cloudy conditions, as they are rejected in Rayleigh-clear conditions at these altitudes (due to being very noisy and not providing positive impact in OSEs).

The zonal average daily number of observations for AMV observations is shown in the bottom left panel in Figure 5. The absence of AMV observations in the mid-latitudes (between $\approx -60°$S to $-20°$S and 20°N to 60°N) in the mid-troposphere is explained by the fact that AMVs are not assimilated between 350 hPa and 800 hPa, mainly because of the uncertainty in the cloud top height. All geostationary winds are also discarded over land above a latitude of 30°. Nonetheless, with this strict quality control, AMVs observations are very numerous between latitudes of approximately -50 to +50. It should be noted that this quality control is not the same in all meteorological centers, and that the number of AMV wind observations could increase if a more sophisticated quality control were applied. Work is on-going at Météo-France to update this quality control.

WIVERN simulated observations (bottom right panel in Figure 5) are located in the troposphere, where there are clouds. As shown in Figure 5, at all latitudes the number of observations made by WIVERN is very large through the entire troposphere. As discussed in subsection 2.4, WIVERN observations are not assimilated below the altitude of

1500 m to avoid ground clutters, which explains the lack of observations at low altitudes above a pressure of ≈ 800 hPa. It should be noted that this criteria is a pessimistic scenario of the future capabilities of WIVERN to observe winds closer to the surface (Manconi et al., 2024), especially over ocean, which could be revisited in the future.

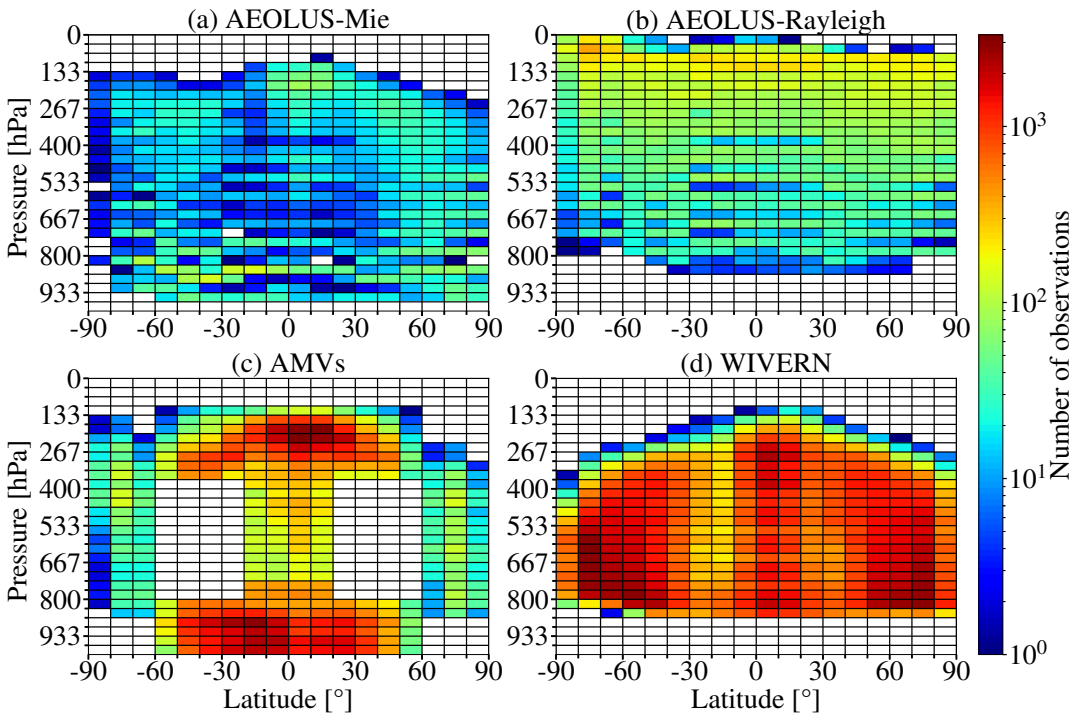

FIGURE 5 2D histograms of the average number of daily assimilated observations, as a function of altitude and latitude. Data are averaged over the period of study of 21 days.

Finally, to summarize Figure 5, Figure 6 shows the daily average vertical distribution of WIVERN (blue), AMV (green), Aeolus-1 in Rayleigh-clear (magenta) and in Mie-Cloudy areas (yellow) in the Northern hemisphere (left), tropics (middle) and in the southern hemisphere (right). In the stratosphere, the number of observations is largely dominated by Aeolus-1. Then, the upper (below a pressure of approximately 300 hPa) and lower (above a pressure of approximately 850 hPa) troposphere are largely dominated by AMV observations. Finally, the mid-troposphere (between approximately 850 hPa and 300 hPa) is mostly covered by the simulated WIVERN observations. This is particularly true in the mid-latitudes as the number of simulated WIVERN observations is more important than in the tropics. Therefore, Figure 6 demonstrates the vertical complementarity between Aeolus-1, AMV and WIVERN observations, especially as WIVERN will provide a large sampling of wind observations within the clouds and precipitations, which are currently poorly covered by other spaceborne wind satellite products on a global scale.

4.3 | Impact on the EDA spread ratio

To assess the impact of Aeolus-1, AMV and WIVERN observations (alone or jointly), the EDA spread ratios are computed for the six EDA experiments (described in subsection 4.1), using the *REF* EDA spread ratio as a reference in

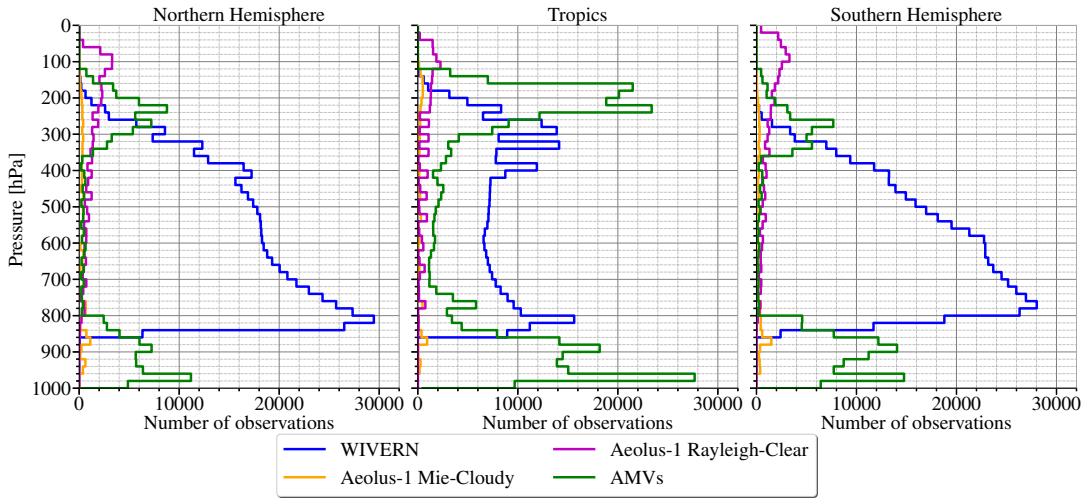

FIGURE 6 Vertical histograms of the averaged number of daily assimilated observations. Data is averaged over the 21 days period.

Equation 8. Figure 7 shows the vertical profiles of the zonal wind I_u, meridional wind I_v, temperature I_T and humidity I_q (from top to bottom) spread ratios. In Figure 7, the profiles are shown for the Northern Hemisphere (left), Southern Hemisphere (right) and for the Tropics (middle). As explained earlier in subsection 3.3, negative values of spread ratios indicate a positive impact of the new observation (e.g. AMVs, Aeolus and/or WIVERN) as their assimilation has led to a reduced uncertainty (e.g. EDA spread) of the 12 hour forecasts.

The EDA experiments in which one of the three type of observations (e.g. AMVs in green, Aeolus in red, WIVERN in blue) are assimilated alone are first inter-compared by the dashed lines in Figure 7. AMVs (green dotted line) has a large positive impact in the lower troposphere between approximately 800 hPa and 900 hPa, for every domain and for all variables (I_u, I_v, I_T and I_q). A similar impact is also highlighted in the upper troposphere at approximately 300 hPa in the mid-latitudes and at approximately 200 hPa in the Tropics. This impact can be directly linked to the large amount of AMV observations at these altitudes, as shown in Figure 5 and Figure 6. These results are also in line with the impacts obtained with the OSE experiments performed at ECMWF (Bormann et al., 2019) and at Météo-France (Chambon et al., 2023). Finally, Figure 7 indicates that the assimilation of AMV wind observations leads to a greater reduction of the forecast uncertainties in the Tropics, then in the Southern Hemisphere, and finally to a less extent in the Northern Hemisphere. It should be noted that these impacts could be different if a more sophisticated data assimilation setup (e.g. quality control and observation error) was followed, as done for the Met-Office NWP model (Forsythe and Saunders, 2008)

The impact of Aeolus-1 observations is positive in all domains, as the zonal spread ratio I_u reaches a value in between approximately -1.5% (NH and Tropics) to -2% (SH) in the troposphere, and is particularly important in the stratosphere, where $I_u \approx -4\%$ in the Tropics and in the Southern Hemisphere. A similar positive impact is also found on the temperature I_T and meridional wind I_v spread ratios. This noticeable impact is due to the uniqueness of Aeolus which provides a large number of clear sky wind observations due to the backscattering of air molecules (Rayleigh diffusion). In addition, there is a limited amount of observations in the stratosphere in the global observing system,

which explains why assimilating Aeolus-1 observations has such a positive impact at these altitudes. This positive impact of Aeolus-1 is consistent with the results found in the Observing System Experiments (OSEs) performed by Pourret et al. (2022) and by Rennie et al. (2021). Finally, it should be noted that the impact of Aeolus-1 on the specific humidity spread ratio I_q is only neutral to slightly positive in the troposphere. It also appears to be very noisy in the stratosphere. This noise is due to the fact that the humidity q is nearly null at these high altitudes, and any analysis on the humidity EDA spread I_q at altitudes $>$ 200 hPa is irrelevant.

The assimilation of simulated WIVERN observations has a significant positive impact in the mid-troposphere (between 800 hPa to 300 hPa), especially in the Northern and Southern Hemispheres, where I_u and I_v are in between -2% and -4%. This can be explained by the ability of WIVERN to provide direct in-cloud wind observations through the entire troposphere and with such a large sampling (see subsection 4.2). Although to a lesser extent, the assimilation of WIVERN in the Tropics also leads to an EDA spread reduction of approximately -2% in the Troposphere. The smaller impact of wivern in the tropics can be explained by the smaller number of assimilated observations in this domain (see Figure 6). Besides, subsection 4.2 demonstrates that the assimilation of WIVERN also benefits the temperature fields as the temperature spread ratio I_T can reach a value of $\approx$ - 2 % in the mid-latitudes. Nontheless, this impact is only neutral in the Tropics. The larger impact in the mid-latitudes on the temperature fields can be explained by the stronger relationship between winds and temperatures at these latitudes. Finally, unlike for Aeolus-1 which is mainly dominated by clear sky observations, the impact of simulated WIVERN and real AMV observations is also significantly positive on the humidity spread ratio I_q. The larger impact of in-cloud wind observations, compared to clear sky observations (e.g. Aeolus-1) on the humidity fields can be related to a stronger correlation between in-cloud winds and mass fields within cloudy areas.

Figure 7 highlights the vertical complementarity in the vertical between the three types of observations. Indeed, the lower (above a pressure of $\approx$ 800 hPa) and upper troposphere are dominated by the AMVs, except in the Northern Hemisphere where the impact of WIVERN is larger as that of AMVs. It should be noted that this result could be modified if WIVERN observations were also assimilated below an altitude of 1500 m (see the quality control in subsection 2.4). The mid-troposphere (between $\approx$ 300 hPa and 800 hPa) is largely dominated by WIVERN and the stratosphere by Aeolus.

Finally, regarding the combined assimilation of "AMVS+AEOLUS" (magenta solid line), "AMVS + WIVERN" (cyan solid line) and "AMVs+AEOLUS+WIVERN (All)" (black solid line), it is important to notice that Figure 7 demonstrates that there is no saturation effect, as I_u and I_v continue to decrease as new wind observations are assimilated on top of others. This is probably due to the uniqueness of WIVERN and Aeolus which provide wind observations in areas that are both poorly covered by other observations on a global scale.

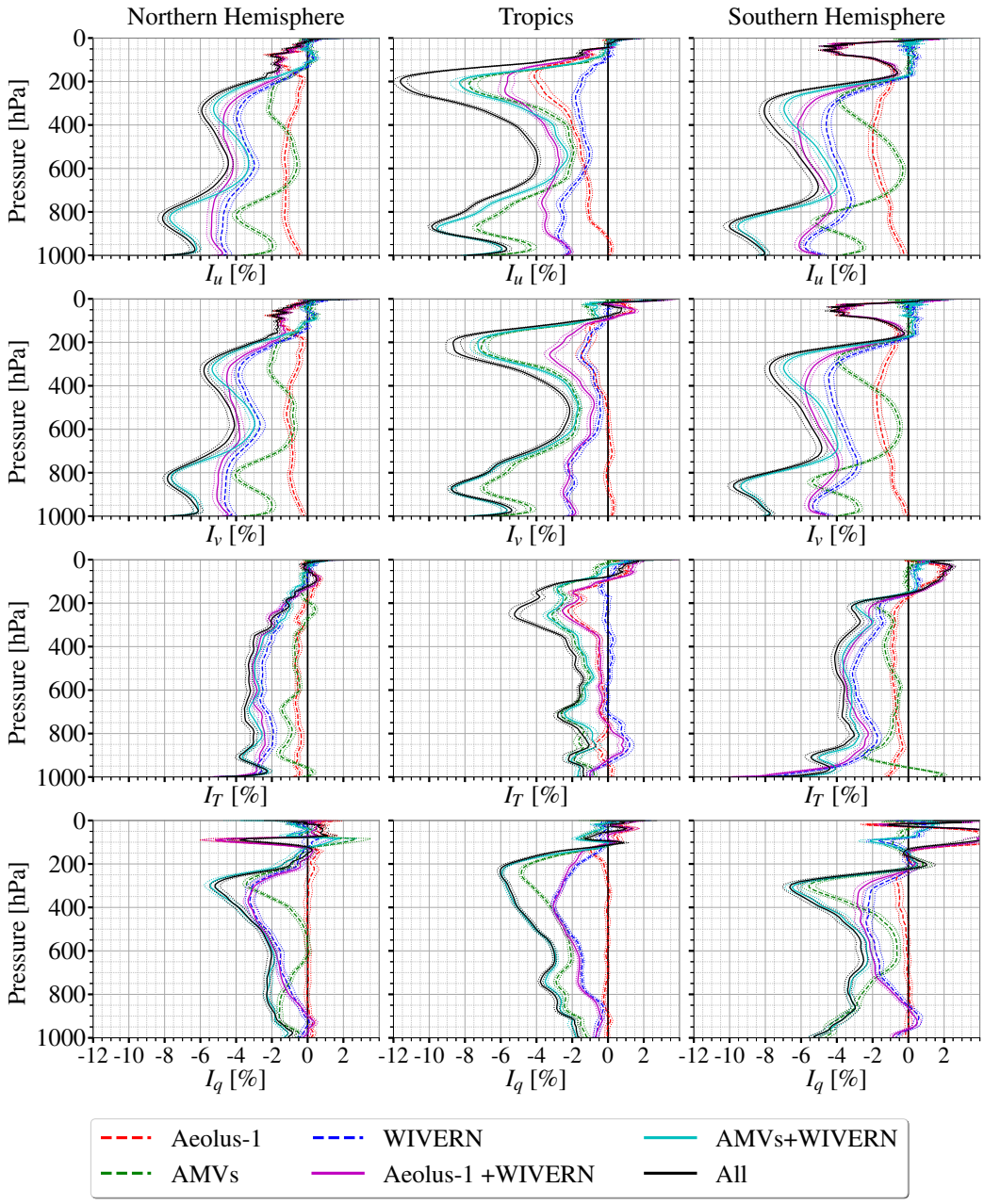

FIGURE 7 Vertical profiles of average spread ratios (21 days) for zonal wind I_u (first row), meridional wind I_v (second row), temperature I_T (third row) and specific humidity I_q (fourth row), for the Northern Hemisphere (left), Tropics (middle) and Southern Hemisphere (right). Dotted lines represent experiments with only one type of observations assimilated, and solid lines experiments with multiple types of observations assimilated. The interval of confidence of 99% is represented by dotted lines surrounding each colored line.

5 | COMPARISONS OF THE IMPACT OF WIVERN VERSUS EPS-AEOLUS

It is proposed here to assimilate simulated EPS-Aeolus observations, in order to assess their impact in terms of EDA spread ratios and their complementarity with WIVERN observations, since both satellites may be operational at the same time. Contrary to the OSSE experiment performed by Marseille et al. (2023), it is important to emphasize that a number of simplifications have been made to simulate EPS-Aeolus as in Healy et al. (2023) and that several proposed new features of EPS-Aeolus are not taken into account in this study (e.g. increased vertical resolution, enhanced signal to noise ratio and capabilities to detect aerosols). Therefore, the impact of EPS-Aeolus is probably underestimated in this study.

5.1 | EPS-Aeolus Data assimilation setup

First, the same methodology as the one employed to simulate Aeolus-1 observations is used to generate EPS-Aeolus observations (see subsection 3.1). The spatial, vertical and temporal binning of simulated EPS-Aeolus are assumed to be the same as for Aeolus-1 for the entire period of study. The thinning and quality control for simulated EPS-Aeolus are also assumed to be the same as for Aeolus-1 (Pourret et al., 2022). To identify the different scenes, a pixel is classified as Mie-Cloudy (resp. Rayleigh-clear) if it is the case in the Aeolus-1 observation dataset. As in Healy et al. (2023), improvements in the signal to noise ratio (SNR) of EPS-Aeolus, which could lead to a larger number of assimilated Mie cloudy observations, have not been considered in this study. Therefore, the number of simulated EPS-Aeolus observations is the same as for Aeolus-1.

Only the observation error specifications are changed for EPS-Aeolus. First, as for Aeolus-1, the observation error standard deviation σ_o is defined as the addition of instrumental error σ_i and representativity error σ_r following Equation 9:

$$\sigma_{o1}^2 = \sigma_{i1}^2 + \sigma_r^2 \tag{9}$$

The representativity error σ_r depends on the meteorological scene observed by Aeolus. It is equal to 2 m.s^{-1} for a Mie-Cloudy observation, and to 0 m.s^{-1} for a Rayleigh-Clear observation (Pourret et al., 2022). Since the NWP model used to simulate EPS-Aeolus is the same as the one used to simulate Aeolus-1 observations, the representativity error remains the same as for Aeolus. The fact that global NWP model will most likely be running at kilometric scale in 2030 will probably lead to an increase in the representativity error for Rayleigh-Clear observations, and a decrease for Mie-Cloudy observations. This effect is not accounted for in this study, as the observations are simulated using the 2021 global NWP model ARPEGE (see subsection 2.2), which is why it has been decided to use the same representativity error for EPS-Aeolus and for Aeolus-1.

For the instrumental error σ_i, instead of using a fixed value which doesn't vary with the vertical nor with the meteorological scene, it has been decided to scale the instrumental error of EPS-Aeolus σ_{i2} as a function of the instrumental error of Aeolus-1 σ_{i1}. Thus, σ_{i2} is derived from σ_{i1} through a scaling factor α:

$$\sigma_{i2} = \alpha \sigma_{i1} \tag{10}$$

The methodology employed to derive α is:

$$\alpha = \frac{\sigma_{tgt}}{\overline{\sigma_{i1}}} \tag{11}$$

where σ_{tgt} is introduced as a target standard deviation for EPS-Aeolus, and $\overline{\sigma_{i1}}$ is the mean value of Aeolus-1 instrumental error which has been calculated over the period of study. Following the specifications of EPS-Aeolus, the target standard deviation error is approximately 2 m.s^{-1}. $\overline{\sigma_{i1}}$ can be obtained through the standard deviation of first-guess departure $\sigma_{fgdepar}$ statistics following :

$$\sigma^2_{fgdepar} = \overline{\sigma_{i1}}^2 + \sigma_r^2 + \sigma_b^2 \tag{12}$$

where σ_b is the global average background error ($\approx$ 2.4 m.s^{-1}), and $\sigma_{fgdepar}$ is approximately equal to 7 m.s^{-1} (resp. 3.9 m.s^{-1}) for Rayleigh-clear (resp. Mie-Cloudy) simulated observations. Note that these average values were calculated using the statistics of the operational deterministic NWP model of Météo-France ARPEGE for this specific period of study (September 2021).

Finally, α is computed in Equation 13:

$$\alpha = \frac{\sigma_{tgt}}{\overline{\sigma_{i1}}} = \frac{\sigma_{tgt}}{\sqrt{\sigma^2_{fgdepar} - \sigma_r^2 - \sigma_b^2}} \tag{13}$$

with standard deviation values indicated in Table 3.

Parameters \ Conditions	Mie-Cloudy	Rayleigh- Clear
$\sigma_{fgdepar}$	3.9 m.s^{-1}	7 m.s^{-1}
σ_r	2 m.s^{-1}	0 m.s^{-1}
σ_b	2.4 m.s^{-1}	2.4 m.s^{-1}
σ_{tgt}	2 m.s^{-1}	2 m.s^{-1}

TABLE 3 Values of the different standard deviation parameters used to derive EPS-Aeolus observation error standard deviations. These statistics have been derived from the operational deterministic NWP model of Météo-France ARPEGE for this specific period of study (September 2021), in which Aeolus-1 is assimilated.

Finally, the observation error standard deviation σ_{o2} for EPS-Aeolus is defined as :

$$\sigma^2_{o2} = \sigma^2_{i2} + \sigma_r^2 = \alpha^2(\sigma^2_{o1} - \sigma_r^2) + \sigma_r^2 \tag{14}$$

Vertical profiles of σ_{o1} and σ_{o2} are shown in Figure 8.

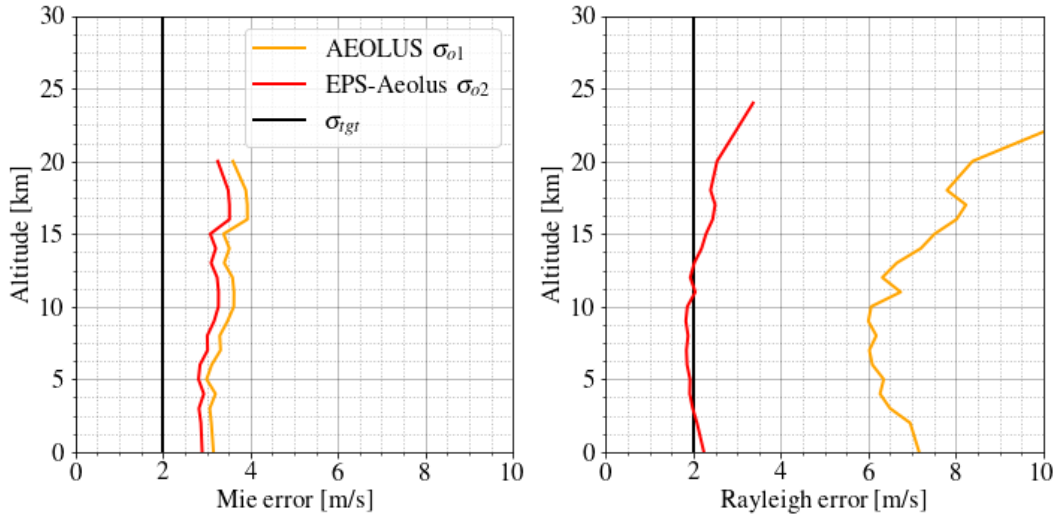

FIGURE 8 Observation error σ_o as a function of altitude, for Mie scattering on the left hand side and Rayleigh scattering on the right hand side. AEOLUS observation error σ_{o1} is plotted in yellow line, and derived EPS-Aeolus observations error $\sigma_o 2$ is plotted in red line. $\sigma_{tgt} = 2$ m.s^{-1} is plotted in black line.

5.2 | EDA experiment

To assess the impact of EPS-Aeolus and its complementarity with WIVERN, a total of four EDA experiments have been performed. They are summarized in Table 4. The EDA spread of each experiment will be compared with the *REF* EDA spread, which assimilates all the observations that are operationally assimilated in ARPEGE, including AMVs (see caption of Table 1 for further details).

Experiment \ Observations	WIVERN	EPS-Aeolus	Aeolus-1	AMVs	Other
REF				x	x
Aeolus-1			x	x	x
EPS-Aeolus		x		x	x
WIVERN	x			x	x
WIVERN + EPS-Aeolus	x	x		x	x

TABLE 4 Description of the observations used in the different experiments. AMV wind observations are derived from geostationnary (METEOSAT, HIMAWARI, GOES) and polar (NOAA, Aqua) satellites. "Other" stands for all the other observations used operationally in the Météo-France ARPEGE model: see Table 1

5.3 | Complementarity between WIVERN and EPS-Aeolus

First of all, the impact EPS-Aeolus has been compared with those of Aeolus-1. In Figure 9 the vertical profiles of spread ratio for simulated EPS-Aeolus and Aeolus-1 observations are shown for the zonal, meridional, temperature and humidity fields (from top to bottom). The impact of EPS-Aeolus (magenta) is greater than that of Aeolus-1 (red), in every domain and at all altitudes. This result is expected as the number of simulated EPS-Aeolus observations is approximately the same as those of Aeolus-1, but with smaller observation errors. Depending on the variable, the EDA spread reduction associated with the assimilation of EPS-Aeolus is about 1.5 to 3 times larger than that of Aeolus-1, which is consistent with the results of the EDA study performed at ECMWF (Healy et al., 2023). The spread reduction in the EPS-Aeolus is particularly large in the stratosphere, due to a large reduction of the observation error of the Rayleigh-Clear observations which are predominant at these altitudes. Finally, in addition to previous pointed causes, it should be noted that the impact of EPS-Aeolus is likely to be underestimated, as EPS-Aeolus is expected to measure more Mie winds than Aeolus-1 in cloudy areas because of its expected improved SNR. Finally, the impact of EPS-Aeolus is neutral on the humidity fields as the humidity spread ratio is close to 0 at all altitude levels.

As shown in the previous section (see section 4), the impact of WIVERN (blue curves) is located in the troposphere and is larger in the mid-latitudes than in the Tropics. Except in the lower troposphere (above a pressure level of approximately 800 hPa), the impact of WIVERN is smaller than that of EPS-Aeolus in the Tropics on the zonal and meridional wind components. In the mid-latitudes, the impact of WIVERN is slightly larger than the impact of EPS-Aeolus in the mid-troposphere (between $\approx$ 200 hPa and $\approx$ 700 hPa), and is much larger in the lower troposphere (above $\approx$ 700 hPa). Vertical profiles of spread ratio on temperature T variable show a significant positive impact of WIVERN in the troposphere in the mid-latitudes and neutral in the Tropics. In particular, except in the Tropics where it is the opposite, the assimilation of WIVERN allows to reduce I_T with a larger order of magnitude than EPS-Aeolus. For the specific humidity q, the impact of WIVERN is also positive through the entire troposphere in the three geographical domains. As explained previously in section 4, the larger impact of WIVERN on these two variables, compared to EPS-Aeolus, could be explained by the strong correlation between the winds and temperature and humidity fields within cloudy areas. Indeed, the spatial and temporal distribution of T and q is highly dependent on advection effects, and this could partly explain the positive impact of WIVERN on these two variables.

Furthermore, Figure 9 highlights the vertical complementarity of the EPS-Aeolus and WIVERN observations, as they allow to reduce the EDA spread at different heights. Moreover, as shown by the green curves in Figure 9, where both simulated observations are assimilated together, their respective impacts seem to be additive.

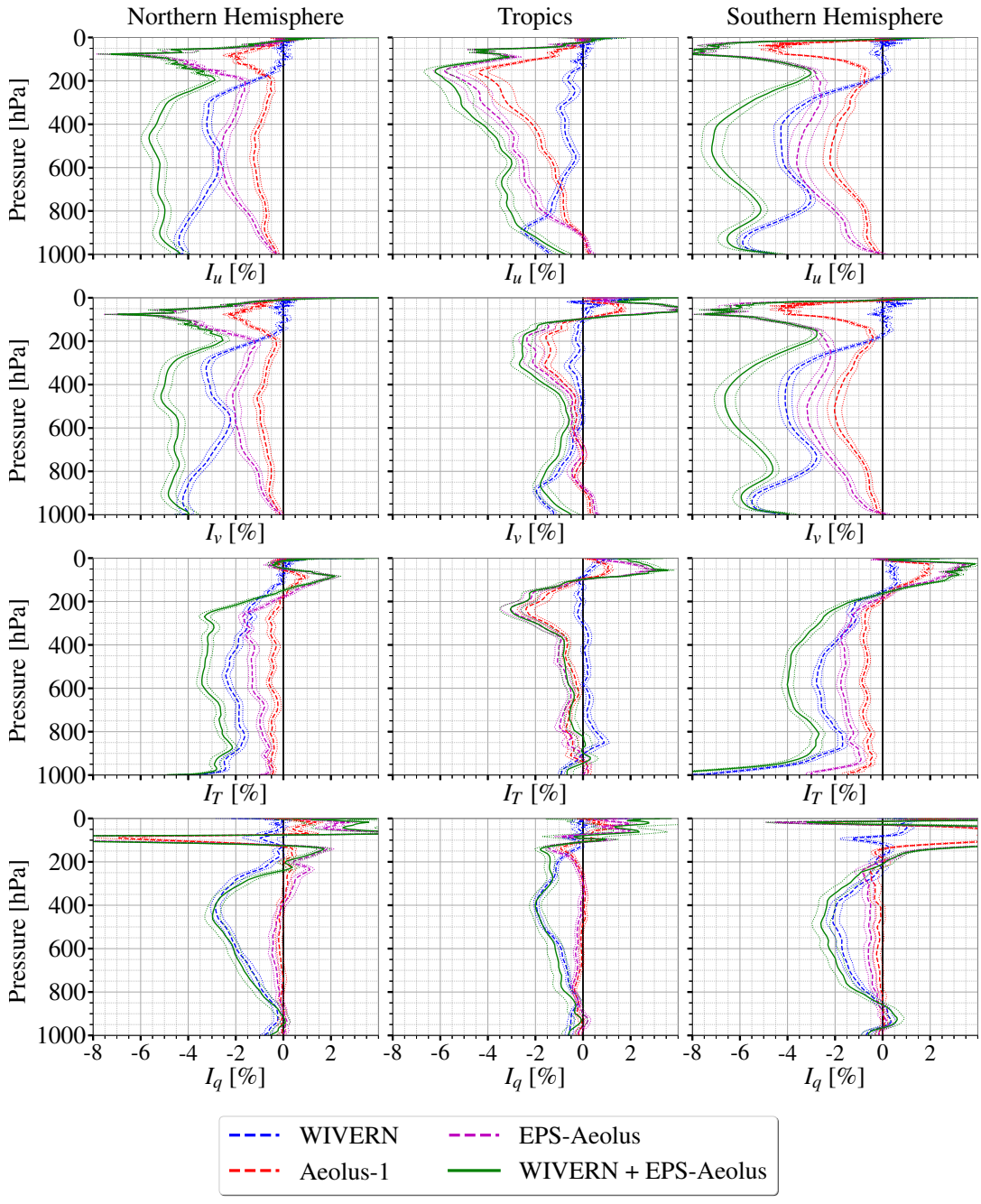

FIGURE 9 Vertical profiles of average spread ratio for zonal and meridional wind I_u and I_v, temperature I_T and humidity I_q. The dotted lines represent the confidence interval of 99% on the mean uncertainty.

6 | CONCLUSIONS AND PERSPECTIVES

As part of the Earth Explorer 11 programme, ESA has selected the WIVERN satellite mission concept to move into phase A in October 2023. With its conically scanning Doppler W-band radar, WIVERN would provide direct wind observations within the clouds, filling a major gap in the Global Observing System within cloudy and precipitation areas. The primary objective of this study was to assess if global NWP model would benefit from the assimilation of WIVERN HLOS winds and to compare these impacts with those obtained through the assimilation of real wind observations, such as Aeolus-1 and AMVs. The second objective of this article was to assess the impact of the EumetSat wind lidar mission EPS-Aeolus, and to demonstrate its complementarity with WIVERN.

For that purpose, the Ensemble of Data Assimilation (EDA) method developed by ECMWF has been set up using the EDA system of the global NWP model ARPEGE (AEARP) for a one-month period in 2021. The main advantage of this impact approach is that simulated WIVERN (or EPS-Aeolus) observations can be assimilated along with real observations from the current Global Observing System. In this method, the impact of a new simulated observation is evidenced by its ability to reduce the ensemble spread (e.g. uncertainty) of the forecasts. The EDA framework built for this study was successfully validated by comparing the impact of real versus simulated Aeolus-1 observations.

The main findings of this EDA impact study are summarized here.

- WIVERN HLOS winds will reduce the uncertainty of the 12-hour wind forecasts by a factor of 3 to 4 % through the entire troposphere in the Northern and Southern Hemispheres, and by a factor of 1 to 2 % in the Tropics. Because of the strong correlation between the wind and temperature within the clouds in the mid-latitudes (e.g. thermal winds), the assimilation of WIVERN HLOS winds will also reduce the uncertainty of the temperature fields by a factor of 2% in the Northern Hemisphere and by 3% in the Southern Hemisphere. Finally, WIVERN also reduce the ensemble humidity spread in the troposphere by a factor of $\approx$ 2% in the three goegraphical domains, which is due to the strong link between wind and humidity fields within cloudy areas. This significant positive impact is explained by the uniqueness of WIVERN observations within the current Global Observing Sytem. Indeed, WIVERN will provide wind observations within the clouds, which are currently poorly observed by other observations of the GOS on a global scale. Besides, the large sampling of WIVERN, which collects observations over a large swath of 800 km, will allow WIVERN to improve NWP model analyses over larger areas than any other existing spaceborne active instrument.
- This study highlighted the strong vertical complementarity between WIVERN, Aeolus and AMV wind observations as they all provide information in complementary areas. In particular, Aeolus leads to major improvements in the stratosphere, AMVs in the lower and upper troposphers, and WIVERN through the mid-troposphere. In addition of this complementarity, there is no saturation effect when WIVERN, AMVs and AEOLUS observations are assimilated jointly, especially as they all provide information in different areas and/or different meteorological situations.
- The assimilation of simulated EPS-Aeolus observations shows, as expected, a larger impact than Aeolus-1. It should be noted that the impact of EPS-Aeolus is underestimated in this study as it does not account for the larger amount of Mie-cloudy winds which will be observed by EPS-Aeolus, compared to Aeolus-1.
- Results also indicate that WIVERN and EPS-Aeolus are highly complementary, as they will measure winds in very distinct areas of the atmosphere. Indeed, while WIVERN will provide a large sampling of cloudy observations through the entire troposphere, EPS-Aeolus will cover very thin clouds and clear-sky areas in the troposphere

and the stratosphere. Finally, results show that there is no saturation effect of the joint assimilation of WIVERN and EPS-Aeolus as the spread ratios keep decreasing when they are both assimilated together. These results are of great interest in the perspective of a simultaneous use of these two active wind satellite missions.

This work opens a broad spectrum of perspectives about the assimilation of WIVERN observations and their use in meteorological applications. It is noticeable that the impact of WIVERN is probably underestimated in this study. First, the W-band reflectivity observed by WIVERN is not assimilated in this study. Recent studies demonstrated the benefits brought by the assimilation of the W-band reflectivity observed by the spaceborne radar CloudSat (Janisková and Fielding, 2020) in the global NWP model of ECMWF. A slightly positive impact of the assimilation of the W-band reflectivity observed by the airborne W-band radar RASTA in the kilometre-scale NWP model AROME was also found by Borderies et al. (2019b). These positive impacts were found with nadir-looking only radars and would therefore be much more significant with WIVERN with its large 800 km cycloid swath. Moreover, the single pulse radar sensitivity used in this study is equal to -15 dBZ; industrial studies show that this figure could be improved by 3 dB, which would allow WIVERN to produce accurate Doppler estimates in thinner clouds. Finally, Duncan et al. (2021) demonstrated that there is no saturation effect of the assimilation of new passive microwave sounding observations in NWP models. Therefore, this may suggest that the assimilation of WIVERN dual-polarisation brightness temperature observations, collected at an unprecedented horizontal resolution of 1km, would likely be beneficial to improve NWP model forecasts.

7 | ACKNOWLEDGEMENTS

This work is a contribution to the WIVERN phase 0 studies which has been supported by the European Space Agency (ESA) under the activities "WInd VElocity Radar Nephoscope (WIVERN) Phase 0 Science and Requirements Consolidation Study (Scirec)" (ESA contract Number) 4000136466/21/NL/LF. We acknowledge the contribution of Jean-François Mahfouf, now retired from Météo-France, who initiated the study under the ESA contract 4000136466/21/NL/LF and who wrote the initial project. The Mission Advisory Group (MAG) members of the phase 0 are acknowledged for there recommendations which helped to improve the results. We would also like to thank Sean Healy for his insightful remarks to simulate and assimilate EPS-Aeolus.

8 | DATA AVAILABILITY STATEMENT

Data can be made available on request.

references

Baker, W. E., Atlas, R., Cardinali, C., Clement, A., Emmitt, G. D., Gentry, B. M., Hardesty, R. M., Källén, E., Kavaya, M. J., Langland, R., Ma, Z., Masutani, M., McCarty, W., Pierce, R. B., Pu, Z., Riishojgaard, L. P., Ryan, J., Tucker, S., Weissmann, M. and Yoe, J. G. (2014) Lidar-measured wind profiles: The missing link in the global observing system:. *Bulletin of the American Meteorological Society*, **95**, 543 – 564. URL: https://journals.ametsoc.org/view/journals/bams/95/4/bams-d-12-00164.1.xml.

Battaglia, A., Martire, P., Caubet, E., Phalippou, L., Stesina, F., Kollias, P. and Illingworth, A. (2022) End to end simulator for the wivern w-band doppler conically scanning spaceborne radar. *Atmospheric Measurement Techniques*, **2021**, 1–31. URL: https://amt.copernicus.org/preprints/amt-2021-342/.

Birman, C., Mahfouf, J.-F., Milz, M., Mendrok, J., Buehler, S. A. and Brath, M. (2017) Information content on hydrometeors from millimeter and sub-millimeter wavelengths. *Tellus A: Dynamic Meteorology and Oceanography*, **69**, 1271562.

Borderies, M., Caumont, O., Delanoë, J., Ducrocq, V. and Fourrié, N. (2019a) Assimilation of wind data from airborne doppler cloud-profiling radar in a kilometre-scale nwp system. *Natural Hazards and Earth System Sciences*, **19**, 821–835.

Borderies, M., Caumont, O., Delanoë, J., Ducrocq, V., Fourrié, N. and Marquet, P. (2019b) Impact of airborne cloud radar reflectivity data assimilation on kilometre-scale numerical weather prediction analyses and forecasts of heavy precipitation events. *Natural Hazards and Earth System Sciences*, **19**, 907–926. URL: https://nhess.copernicus.org/articles/19/907/2019/.

Bormann, N., Lawrence, H. and Farnan, J. (2019) Global observing system experiments in the ecmwf assimilation system. URL: https://www.ecmwf.int/node/18859.

Bouyssel, F., Berre, L., Bénichou, H., Chambon, P., Girardot, N., Guidard, V., Loo, C., Mahfouf, J.-F., Moll, P., Payan, C. et al. (2022) The 2020 global operational nwp data assimilation system at météo-france. *Data Assimilation for Atmospheric, Oceanic and Hydrologic Applications (Vol. IV)*, 645–664.

Chambon, P., Mahfouf, J.-F., Audouin, O., Birman, C., Fourrié, N., Loo, C., Martet, M., Moll, P., Payan, C., Pourret, V. and Raspaud, D. (2023) Global observing system experiments within the météo-france 4d-var data assimilation system. *Monthly Weather Review*, **151**, 127 – 143. URL: https://journals.ametsoc.org/view/journals/mwre/151/1/MWR-D-22-0087.1.xml.

Coopmann, O., Fourrié, N., Chambon, P., Vidot, J., Brousseau, P., Martet, M. and Birman, C. (2023) Preparing the assimilation of the future mtg-irs sounder into the mesoscale numerical weather prediction arome model. *Quarterly Journal of the Royal Meteorological Society*, **149**, 3110–3134. URL: https://rmets.onlinelibrary.wiley.com/doi/abs/10.1002/qj.4548.

Courtier, P., Thépaut, J.-N. and Hollingsworth, A. (1994) A strategy for operational implementation of 4d-var, using an incremental approach. *Quarterly Journal of the Royal Meteorological Society*, **120**, 1367–1387.

Desroziers, G., Pouponneau, B., Thépaut, J.-N., Janisková, M. and Veersé, F. (1999) Four-dimensional variational analyses of fastex situations using special observations. *Quarterly Journal of the Royal Meteorological Society*, **125**, 3339–3358.

Duncan, D. I., Bormann, N. and Hólm, E. V. (2021) On the addition of microwave sounders and numerical weather prediction skill. *Quarterly Journal of the Royal Meteorological Society*, **147**, 3703–3718. URL: https://rmets.onlinelibrary.wiley.com/doi/abs/10.1002/qj.4149.

Duruisseau, F., Chambon, P., Guedj, S., Guidard, V., Fourrié, N., Taillefer, F., Brousseau, P., Mahfouf, J.-F. and Roca, R. (2017) Investigating the potential benefit to a mesoscale nwp model of a microwave sounder on board a geostationary satellite. *Quarterly Journal of the Royal Meteorological Society*, **143**, 2104–2115. URL: https://rmets.onlinelibrary.wiley.com/doi/abs/10.1002/qj.3070.

Eriksson, P., Ekelund, R., Mendrok, J., Brath, M., Lemke, O. and Buehler, S. A. (2018) A general database of hydrometeor single scattering properties at microwave and sub-millimetre wavelengths. *Earth System Science Data*, **10**, 1301–1326.

Forsythe, M. and Saunders, R. (2008) Amv errors: A new approach in nwp. In *Proceedings of the 9th International Wind Workshop, Annapolis, Maryland, USA*, 14–18.

Garrett, K., Liu, H., Ide, K., Hoffman, R. N. and Lukens, K. E. (2022) Optimization and impact assessment of aeolus hlos wind assimilation in noaa's global forecast system. *Quarterly Journal of the Royal Meteorological Society*, **148**, 2703–2716. URL: https://rmets.onlinelibrary.wiley.com/doi/abs/10.1002/qj.4331.

Geer, A., Bauer, P., Lonitz, K., Barlakas, V., Eriksson, P., Mendrok, J., Doherty, A., Hocking, J. and Chambon, P. (2021) Bulk hydrometeor optical properties for microwave and sub-millimetre radiative transfer in rttov-scatt v13. 0. *Geoscientific Model Development*, **14**, 7497–7526.

Hagelin, S., Azad, R., Lindskog, M., Schyberg, H. and Körnich, H. (2021) Evaluating the use of aeolus satellite observations in the regional numerical weather prediction (nwp) model harmonie–arome. *Atmospheric Measurement Techniques*, **14**, 5925–5938. URL: https://amt.copernicus.org/articles/14/5925/2021/.

Harnisch, F., Healy, S., Bauer, P. and English, S. (2013) Scaling of gnss radio occultation impact with observation number using an ensemble of data assimilations. *Monthly Weather Review*, **141**, 4395–4413.

Healy, S., Lean, K., Semane, N. and Bormann, N. (2023) Task 2: Doppler wind lidar eda impact assessment. *EUMETSAT study report (available on request from authors)*.

Horányi, A., Cardinali, C., Rennie, M. and Isaksen, L. (2015) The assimilation of horizontal line-of-sight wind information into the ecmwf data assimilation and forecasting system. part i: The assessment of wind impact. *Quarterly Journal of the Royal Meteorological Society*, **141**, 1223–1232. URL: https://rmets.onlinelibrary.wiley.com/doi/abs/10.1002/qj.2430.

Illingworth, A., Battaglia, A., Bradford, J., Forsythe, M., Joe, P., Kollias, P., Lean, K., Lori, M., Mahfouf, J.-F., Melo, S. et al. (2018) Wivern: A new satellite concept to provide global in-cloud winds, precipitation, and cloud properties. *Bulletin of the American Meteorological Society*, **99**, 1669–1687.

Janisková, M. and Fielding, M. D. (2020) Direct 4d-var assimilation of space-borne cloud radar and lidar observations. part ii: Impact on analysis and subsequent forecast. *Quarterly Journal of the Royal Meteorological Society*, **146**, 3900–3916.

Lean, K., Bormann, N. and Healy, S. (2023) Task 1.1 evaluation of initial future eps-sterna constellations with 50 and 183 ghz. *EUMETSAT Contract Report*.

Lean, K., Bormann, N., Healy, S. and English, S. (2022) Final report: Study to assess earth observation with small satellites and their prospects for future global numerical weather prediction. *ESA Contract Report*. URL: .

Li, L., Žagar, N., Raeder, K. and Anderson, J. L. (2023) Comparison of temperature and wind observations in the tropics in a perfect-model, global enkf data assimilation system. *Quarterly Journal of the Royal Meteorological Society*, **149**, 2367–2385. URL: https://rmets.onlinelibrary.wiley.com/doi/abs/10.1002/qj.4511.

Liu, Z.-Q. and Rabier, F. (2002) The interaction between model resolution, observation resolution and observation density in data assimilation: A one-dimensional study. *Quarterly Journal of the Royal Meteorological Society*, **128**, 1367–1386. URL: https://rmets.onlinelibrary.wiley.com/doi/abs/10.1256/003590002320373337.

Lonitz, K., Marquardt, C., Bowler, N. and Healy, S. (2021) *Final Technical Note of 'Impact assessment of commercial GNSS-RO data'*. URL: https://www.ecmwf.int/node/20240.

Lopez, P. (2002) Implementation and validation of a new prognostic large-scale cloud and precipitation scheme for climate and data-assimilation purposes. *Quarterly Journal of the Royal Meteorological Society: A journal of the atmospheric sciences, applied meteorology and physical oceanography*, **128**, 229–257.

Manconi, F., Battaglia, A. and Kollias, P. (2024) Characterization of surface clutter signal in presence of orography for a space-borne conically scanning w-band doppler radar.

Mangla, R., Borderies, M., Chambon, P., Geer, A. and Hocking, J. (2024) Assessment and application of melting layer simulations for spaceborne radars within the rttov-scatt v13.1 model. *Atmospheric Measurement Techniques Discussions*, **2024**, 1–50. URL: https://amt.copernicus.org/preprints/amt-2024-131/.

Marinescu, P. J., Cucurull, L., Apodaca, K., Bucci, L. and Genkova, I. (2022) The characterization and impact of aeolus wind profile observations in noaa's regional tropical cyclone model (hwrf). *Quarterly Journal of the Royal Meteorological Society*, **148**, 3491–3508. URL: https://rmets.onlinelibrary.wiley.com/doi/abs/10.1002/qj.4370.

Marseille, G.-J., Stoffelen, A. and Rennie, M. (2023) Aeolus and eps-aeolus simulations. URL: https://www-cdn.eumetsat.int/files/2024-04/EUM_KNMI_LIPAS_Aeolus2_OSSE_final.pdf.

Martin, A., Weissmann, M. and Cress, A. (2023) Impact of assimilating aeolus observations in the global model icon: A global statistical overview. *Quarterly Journal of the Royal Meteorological Society*, **n/a**. URL: https://rmets.onlinelibrary.wiley.com/doi/abs/10.1002/qj.4541.

Montmerle, T. and Faccani, C. (2009) Mesoscale assimilation of radial velocities from doppler radars in a preoperational framework. *Monthly Weather Review*, **137**, 1939–1953.

Pazmany, A. L., Galloway, J. C., Mead, J. B., Popstefanija, I., McIntosh, R. E. and Bluestein, H. W. (1999) Polarization diversity pulse-pair technique for millimeter-wavedoppler radar measurements of severe storm features. *Journal of Atmospheric and Oceanic Technology*, **16**, 1900 – 1911. URL: https://journals.ametsoc.org/view/journals/atot/16/12/1520-0426_1999_016_1900_pdpptf_2_0_co_2.xml.

Pourret, V., Šavli, M., Mahfouf, J.-F., Raspaud, D., Doerenbecher, A., Bénichou, H. and Payan, C. (2022) Operational assimilation of aeolus winds in the météo-france global nwp model arpege. *Quarterly Journal of the Royal Meteorological Society*, **148**, 2652–2671.

Raynaud, L., Berre, L. and Desroziers, G. (2012) Accounting for model error in the météo-france ensemble data assimilation system. *Quarterly Journal of the Royal Meteorological Society*, **138**, 249–262.

Reitebuch, O. (2012) *The Spaceborne Wind Lidar Mission ADM-Aeolus*, 815–827. Berlin, Heidelberg: Springer Berlin Heidelberg. URL: https://doi.org/10.1007/978-3-642-30183-4_49.

Rennie, M. P., Isaksen, L., Weiler, F., de Kloe, J., Kanitz, T. and Reitebuch, O. (2021) The impact of aeolus wind retrievals on ecmwf global weather forecasts. *Quarterly Journal of the Royal Meteorological Society*, **147**, 3555–3586.

Ridal, M., Sanchez-Arriola, J. and Dahlbom, M. (2023) Optimal use of radar radial winds in the harmonie numerical weather prediction system. *Journal of Applied Meteorology and Climatology*. URL: https://journals.ametsoc.org/view/journals/apme/aop/JAMC-D-23-0013.1/JAMC-D-23-0013.1.xml.

Rivoire, L., Marty, R., Carrel-Billiard, T., Chambon, P., Fourrié, N., Audouin, O., Martet, M., Birman, C., Accadia, C. and Ackermann, J. (2024) A global observing-system simulation experiment for the eps–sterna microwave constellation. *Quarterly Journal of the Royal Meteorological Society*.

Rizik, A., Battaglia, A., Tridon, F., Scarsi, F., Kötsche, A., Kalesse-Los, H., Maahn, M. and Illingworth, A. (2023) Impact of crosstalk on reflectivity and doppler measurements for the wivern polarization diversity doppler radar. *IEEE Transactions on Geoscience and Remote Sensing*, **61**, 1–14.

Salonen, K., Cotton, J., Bormann, N. and Forsythe, M. (2015) Characterizing amv height-assignment error by comparing best-fit pressure statistics from the met office and ecmwf data assimilation systems. *Journal of Applied Meteorology and Climatology*, **54**, 225 – 242. URL: https://journals.ametsoc.org/view/journals/apme/54/1/jamc-d-14-0025.1.xml.

Simonin, D., Ballard, S. P. and Li, Z. (2014) Doppler radar radial wind assimilation using an hourly cycling 3d-var with a 1.5 km resolution version of the met office unified model for nowcasting. *Quarterly Journal of the Royal Meteorological Society*, **140**, 2298–2314. URL: https://rmets.onlinelibrary.wiley.com/doi/abs/10.1002/qj.2298.

Sippel, J. A., Zhang, F., Weng, Y., Tian, L., Heymsfield, G. M. and Braun, S. A. (2014) Ensemble kalman filter assimilation of hiwrap observations of hurricane karl (2010) from the unmanned global hawk aircraft. *Monthly Weather Review*, **142**, 4559 – 4580. URL: https://journals.ametsoc.org/view/journals/mwre/142/12/mwr-d-14-00042.1.xml.

Tan, D. G., Andersson, E., Fisher, M. and Isaksen, L. (2007) Observing-system impact assessment using a data assimilation ensemble technique: application to the adm–aeolus wind profiling mission. *Quarterly Journal of the Royal Meteorological Society: A journal of the atmospheric sciences, applied meteorology and physical oceanography*, **133**, 381–390.

Tiedtke, M. (1989) A comprehensive mass flux scheme for cumulus parameterization in large-scale models. *Monthly weather review*, **117**, 1779–1800.

Tridon, F., Battaglia, A., Rizik, A., Scarsi, F. E. and Illingworth, A. (2023) Filling the gap of wind observations inside tropical cyclones. *Earth and Space Science*, **10**, e2023EA003099. URL: https://agupubs.onlinelibrary.wiley.com/doi/abs/10.1029/2023EA003099.